Thermal conductivity of suspended single crystal CH3NH3PbI3 platelets at room temperature

Shen, Chao; Du, Wenna; Wu, Zhiyong; Xing, Jun; Ha, Son Tung; Shang, Qiuyu; Xu, Weigao; Xiong, Qihua; Liu, Xinfeng; Zhang, Qing

2017

Shen, C., Du, W., Wu, Z., Xing, J., Ha, S. T., Shang, Q., . . . Zhang, Q. (2017). Thermal conductivity of suspended single crystal CH3NH3PbI3 platelets at room temperature. Nanoscale, 9(24), 8281-8287. doi:10.1039/c7nr01894k

https://hdl.handle.net/10356/141421

https://doi.org/10.1039/c7nr01894k

Thermal Conductivity of Suspended Single Crystal $CH_3NH_3PbI_3$ Platelets at Room Temperature

Chao Shen,[1,5,#] Wenna Du,[2#] Zhiyong Wu,[2] Jun Xing,[3] Son Tung Ha,[3] Qiuyu Shang,[4] Weigao Xu[3], Jun Zhang[1,5], Qihua Xiong,[3,*] Xinfeng Liu,[2,*] and Qing Zhang[4,*]

[1]State Key Laboratory for Superlattices and Microstructures, Institute of Semiconductors, Chinese Academy of Sciences, Beijing 100083, P. R. China

[2]Division of Photonics, CAS Key Laboratory of Standardization and Measurement for Nanotechnology, CAS Center for Excellence in Nanoscience, National Center for Nanoscience and Technology, Beijing 100190, P. R. China

[3]Division of Physics and Applied Physics, School of Physical and Mathematical Sciences, Nanyang Technological University, Singapore 637371

[4]Department of Materials Science and Engineering, College of Engineering, Peking University, Beijing 100871, P. R. China

[5]College of Materials Science and Opto-Electronic Technology, University of Chinese Academy of Science, Beijing 100049, China

[*]Email address: q_zhang@pku.edu.cn, liuxf@nanoctr.cn and qihua@ntu.edu.sg

Abstract

Recently, organic-inorganic lead halide perovskite have gained great attentions for its breakthrough in photovoltaic and opto-electronics. However, its thermal transport properties that affecting device lifetime and stability are still rarely explored. Here, thermal conductivity properties of single crystal $CH_3NH_3PbI_3$ platelets grown by chemical vapor deposition are studied via non-contact micro-photoluminescence (PL) spectroscopy. We develop a measurement methodology and derive expressions suitable for the thermal conductivity extraction for micro-sized perovskite. The room temperature thermal conductivity of $\sim 0.14 \pm 0.02$ W/m·K is extracted from the dependence of the PL peak energy on the excitation laser power and independently measured PL peak temperature coefficient. With changing the film thickness from 80 to 400 nm, thermal conductivity does not show obvious thickness dependence, indicating that the minimal substrate effects due to the advantage of suspended configuration. The ultra-low thermal conductivity of perovskite, especially thin films, suggests promising applications for thermal isolation, such as thermal insulation and thermal electrics.

Keywords: Thermal conductivity, hybrid perovskite, $CH_3NH_3PbI_3$ photoluminescence, platelet

Introduction

Mixed organic–inorganic halides with perovskite crystalline structure such as $CH_3NH_3PbI_3$ have received much attention for their great potentials in low cost, flexible solar cells.[1-4] Due to their high absorption coefficient and large carrier diffusion length, the power conversion efficiency of solution processed perovskite solar cell has reached ~24%, which is close to commercial crystalline silicon solar cells.[5-8] As a semiconductor, perovskites also show engineered wide-band gap, low non-radiative recombination rate and high external quantum efficiency, which are promising for other opto-electronic devices including lasers, LED, photodetector.[7, 9-11] In these opto-electronic devices, knowing the thermal transport properties of active materials is essential for their application. The light irradiation and electric injection inevitably increases device temperature locally due to heating effect, which can enormously influence device performance and lifetime. For instance, in solar cell and lasers, absorbed photon is relaxes its excess energy via generation of hot carriers, which then transfer their kinetic energy to crystal lattice through momentum scattering and induce device temperature increase. In light emitting devices, large local heating effect may occur because of low electric injection efficiency, which induces device temperature increase and hampers emission efficiency of devices. Therefore, for perovskite based opto-electronic devices, better understanding of thermal transport properties of perovskites is important for not only improving device performance, but also exploring new thermal-related applications. However, so far the study on thermal properties of perovskite is still limited.[12, 13] Furthermore, especially

for perovskite micro-sized single crystals, there are limited methods to evaluate its thermal conductivity, although they are frequently used as photodetectors, sensors and micro-laser devices.

In this work, we report an experimental investigation of thermal conduction of $CH_3NH_3PbI_3$ single crystals with the help of confocal micro-photoluminescence (micro-PL) spectroscopy. A measurement methodology and derive expressions suitable for the thermal conductivity evaluation is developed for micro-sized single crystal perovskite samples. High-quality $CH_3NH_3PbI_3$ ($MAPbI_3$) platelet are grown by two-step chemical vapor deposition (CVD) method. The room temperature value of thermal conductivity is extracted from laser power dependent PL peak energy. The thermal conductivity value κ is evaluated to be 0.14 ± 0.02 W/m·K at room temperature and this value shows little difference with different thickness from 80 to 400 nm.

Results and discussion

High quality $MAPbI_3$ nanoplatelets are synthesized by a home-built vapor phase deposition system with a standard two-step preceding reported in our previous literatures. As shown in **Figure 1a**, PbI_2 powder (99.999%, Aldrich) source and pre-cleaned SiO_2/Si substrate were placed into a quartz tube installed on the home-built vapor phase deposition equipment. The temperature and pressure inside the quartz tube were set and stabilized at 380 °C and 200 Torr for 20 min with a continuous flow of high purity Ar premixed with 5% H_2 gas. The furnace was allowed

to cool down naturally to ambient temperature. The PbI_2 platelets was then transferred onto SiO_2 substrate patterned with hole arrays. To prepare substrate with holes, we first patterns a layer of resist on a SiO_2/Si wafer using photolithography, and then transfer the pattern to the substrate using a potassium hydroxide wet etching and reactive ion etching (RIE). The PbI_2 platelets sitting SiO_2/Si substrate were then put into fresh quartz tube together with methyl ammonium iodide (MAI) located in the center area. The intercalation of methyl ammonium halide molecules via gas-solid hetero-phase reaction was carried out at 115 °C for 2 hours under a pressure of 50 Torr to convert the suspended PbI_2 platelet to $CH_3NH_3PbI_3$.[14] The furnace was allowed to cool down naturally to ambient temperature.

The structure and morphology is characterized by scanning electron miscopy (SEM), atomic force microscopy (AFM) and optical microscopy. **Figure 1B** are SEM images of the as-synthesized PbI_2 platelets on SiO_2/Si substrate, illustrating that dominant PbI_2 platelets and small portion of bulk crystals are simultaneously grown on the silicon oxide surface. The platelets show highly flat and smooth facets with surface roughness of ±1.5 nm measured by AFM (**Figure 1E**). The SEM image of individual PbI_2 platelet on as-prepared Si substrate with hole arrays (**Figure 1B, inset)** suggests that one PbI_2 platelet suspend over several holes in the silicon substrate, which are used to probe thermal conductivity in the further work. **Figure 1C and D** show the optical images of individual PbI_2 platelet (bright green) and converted $MAPbI_3$ platelet (brown). The thickness of the $CH_3NH_3PbI_3$ platelets, measured by atomic force microscopy (AFM) was about 1.8 times of that of corresponding PbI_2

platelets. It agrees well with the ratio of the *c* lattice constant between the two compounds reported in previous studies, suggesting the successful conversion of PbI_2 to $MAPbI_3$.

To confirm the fully conversion of PbI_2 to perovskite, Raman spectra of these samples before and after conversion were conducted. In the measured range of 10 to 160 cm^{-1}, the Raman spectra reveal four distinct bands at ~14, 70, 94, and 110 cm^{-1} as shown in **Figure S3**, which indicate that the $CH_3NH_3PbI_3$ platelets maintain the 4H polytype of PbI_2. The phonon vibration located at ~14 cm^{-1} was assigned to E_2^3, the shear-motion rigid-layer mode of PbI_2 with 4H polytype, while the Raman peaks at ~70, 94, and 110 cm^{-1} were assigned to E_2^1, A_1^1 and A_1^2, respectively. **Figure 2A** shows x-ray diffraction pattern and optical microscopy images (inset) of as-synthesized PbI_2 platelet (upper panel) and $MAPbI_3$ platelets after MAI intercalation (bottom panel). Before conversion, due to the hexagonal structure of PbI_2, the XRD patterns exhibit four strong peaks at ~12.6°, 25.4°, 38.6° and 52.2°, which are corresponding to crystal direction 001, 002, 003 and 004, which is in good agreement with previous studies. After conversion, the identical peaks disappeared, and several other peaks from tetragonal $CH_3NH_3PbI_3$ were detected as shown in the below part of **Figure 2**.[15] The XRD pattern suggests a crystalline structure of the as-grown perovskite. Peaks from PbI_2 disappear suggesting the fully conversion from PbI_2 to $CH_3NH_3PbI_3$. Fringe spacing (0.31 nm, see inset of **Figure 2C**) matches well with the inter-planar spacing of the (220) plane from the tetragonal $CH_3NH_3PbI_3$ crystal, while the fringe spacing of 0.70 nm in inset of **Figure 2B** matches well to the

inter-planar spacing of the (001) plane of the tetragonal PbI_2. Moreover, the absorption (blue dots) and PL (orange squares) spectroscopy of PbI_2 and $CH_3NH_3PbI_3$ platelets at room temperature also indicates successful conversion of PbI_2 to $CH_3NH_3PbI_3$ (see **Figure 2B and C**). The absorption and PL spectroscopy of PbI_2 platelets suggests absorption edge around 500 nm and single PL peak with Gaussian profile centered at ~500 nm **(Figure 2B)**. In $MAPbI_3$ (**Figure 2C),** the absorption edge and PL emission moves located at ~770 nm, which is consistent with band edge emission of $CH_3NH_3PbI_3$.[14] The conversion time from PbI_2 to $CH_3NH_3PbI_3$ was optimized to be 2 hours with the help of X-ray diffraction (XRD) study (**Figure S2)**. When the conversion time was too short (~ 1h)，the PbI_2 and $CH_3NH_3PbI_3$ coexisted from the XRD pattern. With the advance of time, the PbI_2 peaks totally disappear at the conversion complete stage.

In semiconductors, electronic and phonon structure including band gap and phonon energy is highly dependent on temperature. For example, with the increasing of temperature, semiconductor band gap become narrower because of the lattice expansion. Therefore, band edge PL and Raman modes can be used as the temperature indicator.[16, 17] Both of PL and Raman spectroscopy are considered as reliable, non-contact methods to probe local temperature of semiconductors. However, $CH_3NH_3PbI_3$ has low Raman scattering cross section. To do efficient temperature measurement via Raman spectroscopy, excitation laser energy may be too high to destroy sample. Considering outstanding emission properties of $CH_3NH_3PbI_3$, confocal PL microscopy is adopted to measure local temperature.

Figure 3A shows temperature dependent PL spectroscopy of individual $MAPbI_3$ platelet. The power of pump laser (λ=532 nm) was kept as low as 5 μW to minimize the laser heating effect. As temperature increases from 280 to 330 K, the $MAPbI_3$ platelet on SiO_2 substrate exhibits single emission peak due to band-edge emission, which shifts monotonically from 771 nm (1.608 eV) to 767 nm (1.617 eV) (**Figure 3A**). The PL peak position shows blue shift with the increasing of temperature. The widely-observed temperature dependent behavior in perovksite is different from that in transitional technological-important semiconductors such as Si and GaAs [18,19]. The possible reason is the electron-phonon coupling and will be discussed in future. The PL peak center energy E of $CH_3NH_3PbI_3$ is extracted out and plotted versus temperature T (**Figure 3B)**, which could be well fitted as a linear function of $E=E_0+\alpha \cdot T$. The coefficient α is 0.16±0.02 meV/K within the temperature range from 280 K to 330 K. The linear PL emission energy as a function with temperature allows us to easily monitor local temperature fluctuation by PL spectroscopy.

In order to measure the thermal conductivity properties, the $MAPbI_3$ platelet was then suspended to build an isolated thermal system to eliminate influence of environment thermal conduction (**Figure 3C**). First of all, we conducted a detailed analysis on the thermal dynamics for the isolated $MAPbI_3$ system. In absorption and emission process, the absorbed photons stimulate hot carriers with non-zero kinetic energy, which then decay quickly to band edge and transfer their kinetic energy to the lattice through scattering before recombination. Thermal equilibrium process of photon generated hot carriers results in heating of samples. The heat can be

transported by three pathways: material conduction, gas convection and radiation. In our case, the samples locate in vacuum and have small temperature differences with environment, thus the gas convection and radiation can be negligible. Therefore, the laser generated heat in the suspended area can only dissipate by conducting to surrounding area along the platelet itself. According to Fourier's law, the thermal conduction through cross-section of suspended sample is $Q = -\kappa \iint \nabla T \cdot dS$, where Q is heating power per unit time, κ is thermal conductivity, ∇T is temperature gradient of the cross sectional area element *dS*. As shown in **Figure 3D**, since SiO_2/Si substrate can be taken as a thermal reservoir, the temperature increase of non-suspended area is small and undetectable. As a result, the temperature rise is strictly confined in suspended area. After integrating differential form of Fourier's law from excitation spot to the edge of suspended area in a two-dimensional circular geometry, the thermal conductivity can be written as, $\kappa = \gamma \cdot (Q / \Delta T)$, where $\gamma = \ln(R_2 / R_1) / 2\pi h$ is structure factor, ΔT is the energy difference between excitation laser spot position and laser heated area and thermal reservoir. R_1, R_2, h is excitation laser spot diameter, hole diameter and sample thickness, respectively. For a typical sample and thermal system, the structure factor is a constant. The temperature difference between excitation spot and thermal reservoir ΔT is linear to excitation laser power. Therefore, thermal conductivity can be expressed as following equation: $\kappa = \gamma \cdot (Q_1 - Q_2) / (T_{i1} - T_{i2})$, where T_{i1} and T_{i2} are the laser excited area temperatures under heating powers Q_1 and Q_2, respectively. According to above equation, the thermal conductivity can be extracted out directly from power dependent photoluminescence spectroscopy.

Next, power dependence of PL spectroscopy of suspended $MAPbI_3$ platelets is conducted. A 532 nm solid state laser is adopted to obtain strong emission and ensure high heat effect according to $MAPbI_3$ absorption spectroscopy. For ultraviolet lasers, the heat is too strong to damage the sample even under low power; for longer wavelength lasers, the heating effect is too small to be detected. The laser power was kept below 35 μW in our experiments to exclude band filling effect induced peak shift.[20] The laser spot radius is ~0.5 μm. As shown in **Figure 4A-B**, when excitation laser power P increases from 10 μW to 35 μW, the PL peak shifts from 764.24 nm (*c.a.* E_{PL} =1.622 eV) to766.48 (*c.a.* E_{PL} =1.617 eV). According to temperature dependent PL spectroscopy (Fig. 3B), the peak shifts suggests temperature increase of 29.6 K. The PL emission energy is extracted out, which can be well fitted by a linear function of laser power P (**Figure 4C)**. The slope is $\delta E_{PL}/\delta P$=0.26±0.01 meV/μW.

The effective power of laser excitation Q that contributes to thermal energy or temperature increase of $MAPbI_3$ is then evaluated. Firstly, the Equilibrium carriers near to band carriers loss their energy through three recombination processes: non-radiative, radiative, and Auger. For non-radiative and Auger processes, carriers energy will converted to lattice vibration; while for radiative process, the carrier energy will escape as photons. The laser excitation induced heating power Q can be written as $Q = P \cdot \beta$, where P is laser power, β is the heating factor. The heating factor β can be written as $\beta = p \cdot (\eta \cdot (E_{laser} - E_{PL}) / E_{PL} + (1 - \eta))$; where E_{laser} = 2.33 eV and E_{PL} = 1.61 eV are respectively the laser photon energy and the averaged PL photon energy; p is absorption rate, η is quantum yield. The PL quantum efficiency of $CH_3NH_3PbI_3$ is

~90 ±5 % in our measurement because of the relatively small non-radiative and Auger rate.[21] The room temperature absorption coefficient of $CH_3NH_3PbI_3$ at 532 nm is about 5.5×10^4 cm^{-1}, and the calculated absorption p is about 82% for 300 nm platelets, which is in agreement with our absorption measurement using micro-spectrometer.[9] Thus, a heating factor of $\beta = 0.31\pm0.1$ is deduced which can be used to calculate heating power. Combining the temperature coefficient of emission peaks shift $\alpha = \delta E/\delta T = 0.16\pm0.01$ meV/K, heating factor $\beta = 0.31\pm0.01$ and the structure factor $\gamma = (7\pm1)\times10^5$ m^{-1}, we obtained averaged thermal conductivity value to be $\kappa = 0.14\pm0.02$ W/m·K.

To have a further understanding, we have measured the thermal conductivity of $CH_3NH_3PbI_3$ platelets with different thickness from ~80 to 400 nm, as shown in **Figure 5.** The value of thermal conductivity keeps almost constant (~0.14 W/m·K) in the range of 80-400 nm. Two obvious features can be concluded from the thickness dependent measurement of thermal conductivity. Firstly, the measured values of ~0.14 W/m·K were at the same magnitude of single crystals of perovskite (0.5 W/m·K by Pisoni *et al.*;[12] 0.3 W/m·K by Guo *et al.*;[22] 0.59 W/m·K by Qian *et al.*[23]) as reported in previous literature; however, slightly smaller than these reported values. The interface effect should play an important role in the thermal transport behavior due to the suspended platelet configuration without any substrates in our experiments. For the same reason, Guo *et al*. observed the reduction of thermal conductivity on Al_2O_3 substrate compared with that on Si substrate.[22] Secondly, the thermal conductivity shows no dependence on the layer thickness. This independence behavior

demonstrates the phonon surface scattering take almost no effects in this thickness range (80-400 nm). Furthermore, the grain boundary scattering induced by the morphological disorder can also be excluded because of the single crystal structure of our samples. Therefore, the thickness independence of thermal conductivity indicates that the uniformity of the as-grown perovskite single crystal platelet.

Conclusion

In summary, we reported a non-contact optical method to measure thermal conductivity of single crystal $MAPbI_3$ platelets. A measurement methodology and derive expressions suitable for thermal conductivity evaluation for micro-sized perovskite are explored. The substrate effect is minimized due to the advantage of suspended configuration. Using this expression, thermal conductivity at room temperature of κ=0.14±0.02 W/m·K is obtained for two-step CVD grown $MAPbI_3$. The thermal conductivity does not change with nanoplatelets thickness, suggesting that the uniformity of as-prepared perovskite platelets. The ultra-low thermal conductivity indicates that the $MAPbI_3$ platelets can be a promising candidate, especially very thin films, for thermal insulation and thermal electrics related usage.

Experimental methods

The crystalline structure and morphology are characterized by Atomic Force Microscope (Veeco Dimension V), scanning electron microscopy (SEM, JEOL 7001F), X-ray diffraction (XRD; Bruker D8-Advance) and TEM (FEI Tecnai F20). A WITec alpha300 RAS Raman system with a piezo crystal controlled scanning stage, an objective lens of 100× magnification (numerical aperture, NA =0.95), and an

Electron Multiplying CCD was used for recording Raman spectra. All the Raman spectra were recorded under an excitation laser of 532 nm (E laser = 2.33 eV). Micro-PL spectroscopy of individual platelets is conducted by confocal triple-grating spectrometer (Horiba-JY T6400) in a backscattering configuration. Micro-absorption spectra from single perovskite platelet are measured on a home-made micro-based measurement system. A 532 nm solid state laser is focused by an objective (Nikon, 50×, NA=0.45) and excites on platelets with beam diameter of ~1μm. The PL emission signal is collected by the same objective and dispersed by monochromator with 600 g/cm grating and then analyzed by liquid helium cooled charge-coupled device (CCD, Princeton Instruments). A 532 nm long-pass filter is used to block excitation laser line. Continuous-flow microscopy cryostat is used for low-temperature PL spectra measurement. The SiO_2/Si substrate with platelets was pasted onto sample stage using GE vanish (Oxford Bearings Limited Company).

Acknowledgements

Q.Z acknowledges the support of start-up funding from Peking University, one-thousand talent programs from Chinese government, open research fund program of the state key laboratory of low-dimensional quantum physics. X.F.L thanks the support from the Ministry of Science and Technology (No.2016YFA0200700), National Natural Science Foundation of China (No.21673054), Key Research Program of Frontier Science, CAS (No.QYZDB-SSW-SYS031) and Open Project of Key Laboratory for UV-emitting Materials and Technology of Ministry of Education (130028699). C.S thanks the support from NSFC Grant No. 11404324.

References

(1) Lee, M. M.; Teuscher, J.; Miyasaka, T.; Murakami, T. N.; Snaith, H. J. Efficient Hybrid Solar Cells Based on Meso-Superstructured Organometal Halide Perovskites. *Science* **2012**, 338, 643-647.

(2) Burschka, J.; Pellet, N.; Moon, S. J.; Humphry-Baker, R.; Gao, P.; Nazeeruddin, M. K.; Gratzel, M. Sequential deposition as a route to high-performance perovskite-sensitized solar cells. *Nature* **2013**, 499, 316-9.

(3) Liu, M. Z.; Johnston, M. B.; Snaith, H. J. Efficient planar heterojunction perovskite solar cells by vapour deposition. *Nature* **2013**, 501, 395-8.

(4) Heo, J. H.; Im, S. H.; Noh, J. H.; Mandal, T. N.; Lim, C. S.; Chang, J. A.; Lee, Y. H.; Kim, H. J.; Sarkar, A.; Nazeeruddin, M. K.; Gratzel, M.; Seok, S. I. Efficient inorganic-organic hybrid heterojunction solar cells containing perovskite compound and polymeric hole conductors. *Nat Photonics* **2013**, 7, 487-492.

(5) Park, N.-G.; Grätzel, M.; Miyasaka, T.; Zhu, K.; Emery, K. Towards stable and commercially available perovskite solar cells. *Nature Energy* **2016**, 1, 16152.

(6) Bi, D.; Yi, C.; Luo, J.; Décoppet, J.-D.; Zhang, F.; Zakeeruddin, Shaik M.; Li, X.; Hagfeldt, A.; Grätzel, M. Polymer-templated nucleation and crystal growth of perovskite films for solar cells with efficiency greater than 21%. *Nature Energy* **2016**, 1, 16142.

(7) Yuan, M.; Quan, L. N.; Comin, R.; Walters, G.; Sabatini, R.; Voznyy, O.; Hoogland, S.; Zhao, Y.; Beauregard, E. M.; Kanjanaboos, P.; Lu, Z.; Kim, D. H.; Sargent, E. H. Perovskite energy funnels for efficient light-emitting diodes. *Nat Nano* **2016**, 11, 872-877.

(8) Yang, W. S.; Noh, J. H.; Jeon, N. J.; Kim, Y. C.; Ryu, S.; Seo, J.; Seok, S. I. High-performance photovoltaic perovskite layers fabricated through intramolecular exchange. *Science* **2015**, 348, 1234-1237.

(9) Xing, G. C.; Mathews, N.; Lim, S. S.; Yantara, N.; Liu, X. F.; Sabba, D.; Gratzel, M.; Mhaisalkar, S.; Sum, T. C. Low-temperature solution-processed wavelength-tunable perovskites for lasing. *Nat Mater* **2014**, 13, 476-480.

(10) Zhang, Q.; Ha, S. T.; Liu, X.; Sum, T. C.; Xiong, Q. Room-Temperature Near-Infrared High-Q Perovskite Whispering-Gallery Planar Nanolasers. *Nano Letters* **2014**, 14, 5995-6001.

(11) Niu, L.; Zeng, Q.; Shi, J.; Cong, C.; Wu, C.; Liu, F.; Zhou, J.; Fu, W.; Fu, Q.; Jin, C.; Yu, T.; Liu, X.; Liu, Z. Controlled Growth and Reliable Thickness-Dependent Properties of Organic–Inorganic Perovskite Platelet Crystal. *Advanced Functional Materials* **2016**, 26, 5263-5270.

(12) Pisoni, A.; Jaćimović, J.; Barišić, O. S.; Spina, M.; Gaál, R.; Forró, L.; Horváth, E. Ultra-Low Thermal Conductivity in Organic–Inorganic Hybrid Perovskite CH3NH3PbI3. *The Journal of Physical Chemistry Letters* **2014**, 5, 2488-2492.

(13) Naikaew, A.; Prajongtat, P.; Lux-Steiner, M. C.; Arunchaiya, M.; Dittrich, T. Role of phase composition for electronic states in CH3NH3PbI3 prepared from CH3NH3I/PbCl2 solution. *Applied Physics Letters* **2015**, 106.

(14) Ha, S. T.; Liu, X. F.; Zhang, Q.; Giovanni, D.; Sum, T. C.; Xiong, Q. H.

Synthesis of Organic-Inorganic Lead Halide Perovskite Nanoplatelets: Towards High-Performance Perovskite Solar Cells and Optoelectronic Devices. *Adv Opt Mater* **2014**, 2, 838-844.

(15) Baikie, T.; Fang, Y.; Kadro, J. M.; Schreyer, M.; Wei, F.; Mhaisalkar, S. G.; Graetzel, M.; White, T. J. Synthesis and crystal chemistry of the hybrid perovskite (CH3NH3)PbI3 for solid-state sensitised solar cell applications. *Journal of Materials Chemistry A* **2013**, 1, 5628-5641.

(16) Zhang, J.; Li, D. H.; Chen, R. J.; Xiong, Q. H. Laser cooling of a semiconductor by 40 kelvin. *Nature* **2013**, 493, 504-508.

(17) Wehrenfennig, C.; Liu, M. Z.; Snaith, H. J.; Johnston, M. B.; Herz, L. M. Charge carrier recombination channels in the low-temperature phase of organic-inorganic lead halide perovskite thin films. *Apl Mater* **2014**, 2.

(18) Odonnell, K. P.; Chen, X. Temperature-Dependence of Semiconductor Band-Gaps. *Applied Physics Letters* **1991**, 58, 2924-2926.

(19) Yu, C. L.; Chen, Z.; Wang, J. J.; Pfenninger, W.; Vockic, N.; Kenney, J. T.; Shum, K. Temperature dependence of the band gap of perovskite semiconductor compound CsSnI3. *J Appl Phys* **2011**, 110.

(20) Liu, X.; Zhang, Q.; Yip, J. N.; Xiong, Q.; Sum, T. C. Wavelength Tunable Single Nanowire Lasers Based on Surface Plasmon Polariton Enhanced Burstein–Moss Effect. *Nano Letters* **2013**, 13, 5336-5343.

(21) Wehrenfennig, C.; Eperon, G. E.; Johnston, M. B.; Snaith, H. J.; Herz, L. M. High Charge Carrier Mobilities and Lifetimes in Organolead Trihalide Perovskites. *Adv Mater* **2014**, 26, 1584-1589.

(22) Luo, Z. G. S. J. Y. J. S. M. P. V. K. a. T. Structural Phase- and Degradation-Dependent Thermal Conductivity of CH3NH3PbI3 Perovskite Thin Films. *J. Phys. Chem. C* **2016**, 120, 8.

(23) Xin Qian, X. G., and Ronggui Yang. Lattice thermal conductivity of organic-inorganic hybrid perovskite CH3NH3PbI3. *Applied Physics Letters* **2016**, 108.

Figure and Caption

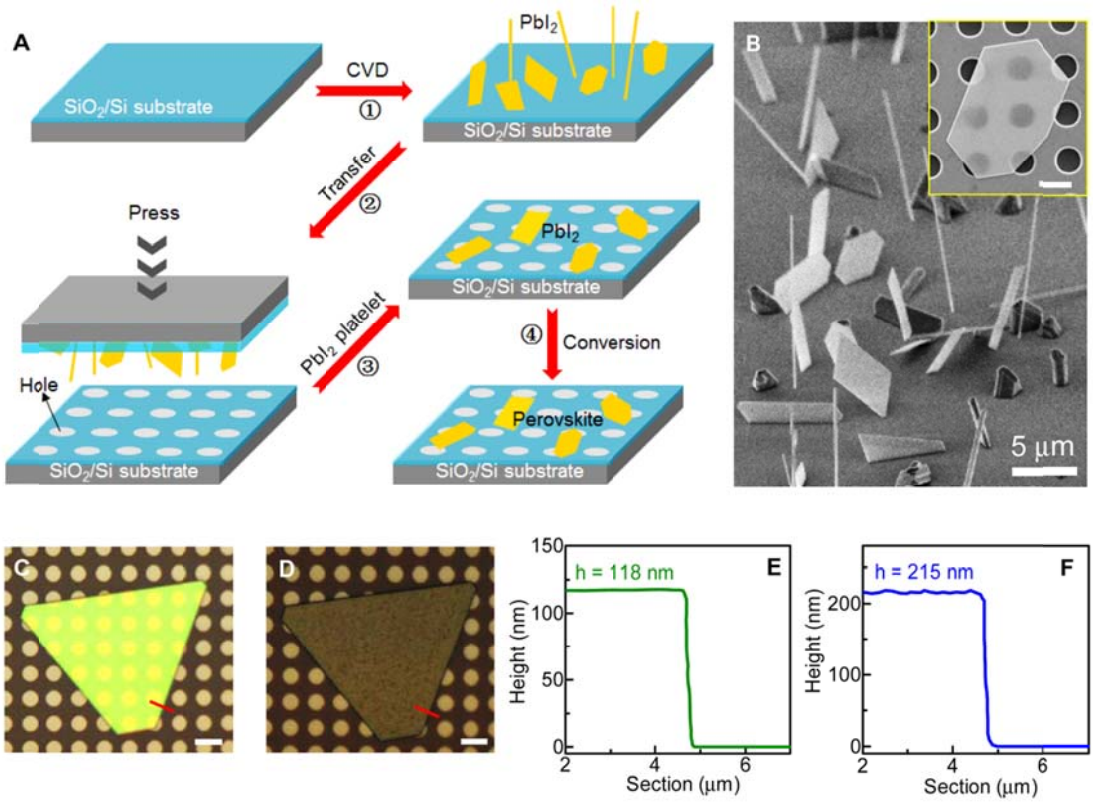

Figure 1 (A) Schematic illustration of the preparation procedures of the perovskite platelets on hole arrays: PbI_2 platelets being grown on SiO_2/Si substrate; Transferring the PbI_2 platelets on SiO_2 substrate onto the as-prepared Si substrate with hole arrays; Converting the suspended PbI_2 platelet to $CH_3NH_3PbI_3$. **(B)** SEM image of PbI_2 platelets grown on SiO_2/Si substrate. The inset shows SEM image of after being converted to $CH_3NH_3PbI_3$. The scale bar inside the image is 5 μm. **(C)-(D)** Optical images of individual PbI_2 platelet and corresponding converted product of $CH_3NH_3PbI_3$ platelet. **(E)-(F)** Thickness of PbI_2 platelet and $CH_3NH_3PbI_3$ platelet in (C) and (D) by AFM characterization. Note that the difference in color for the PbI_2 platelets and $CH_3NH_3PbI_3$ platelet corresponding to the difference in thickness (as measured by AFM). The thickness of the $CH_3NH_3PbI_3$ platelets was about 1.8 times higher compared to the corresponding PbI_2 platelets, which agrees well with the ratio of the c lattice constant between the two compounds.

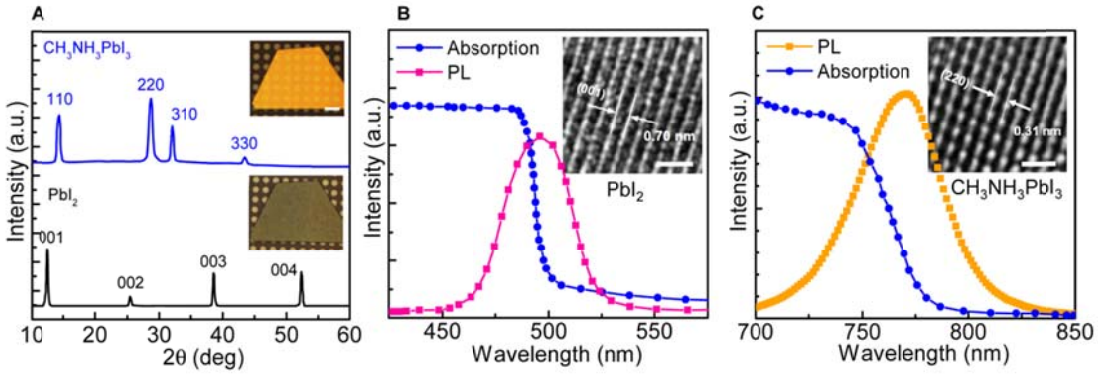

Figure 2 (A) XRD pattern of the as-grown CVD synthesized PbI_2 platelets (above) and after conversion to $CH_3NH_3PbI_3$ platelets (below). After conversion, identical peaks of PbI_2 (001, 002, 003, 004) disappeared, and several peaks belong to tetragonal $CH_3NH_3PbI_3$ were detected. The upper inset shows the microscope photo of one as-grown PbI_2 platelet and the lower inset is the photo of the same platelet after conversion. **(B)** The absorption and PL spectra of single PbI_2 platelets. Inset is a high-resolution TEM (HRTEM) image showing the lattice of crystal. Fringe spacing of 0.70 nm matches well to the inter-planar spacing of the (001) plane of the hexagon PbI_2. The scale bar inside the image is 1 nm. **(C)** The absorption and PL spectra of single $CH_3NH_3PbI_3$ platelets. Inset is a HRTEM image showing the lattice of crystal. Fringe spacing of 0.31 nm matches well to the inter-planar spacing of the (220) plane of the tetragonal $CH_3NH_3PbI_3$. The scale bar inside the image is 1 nm.

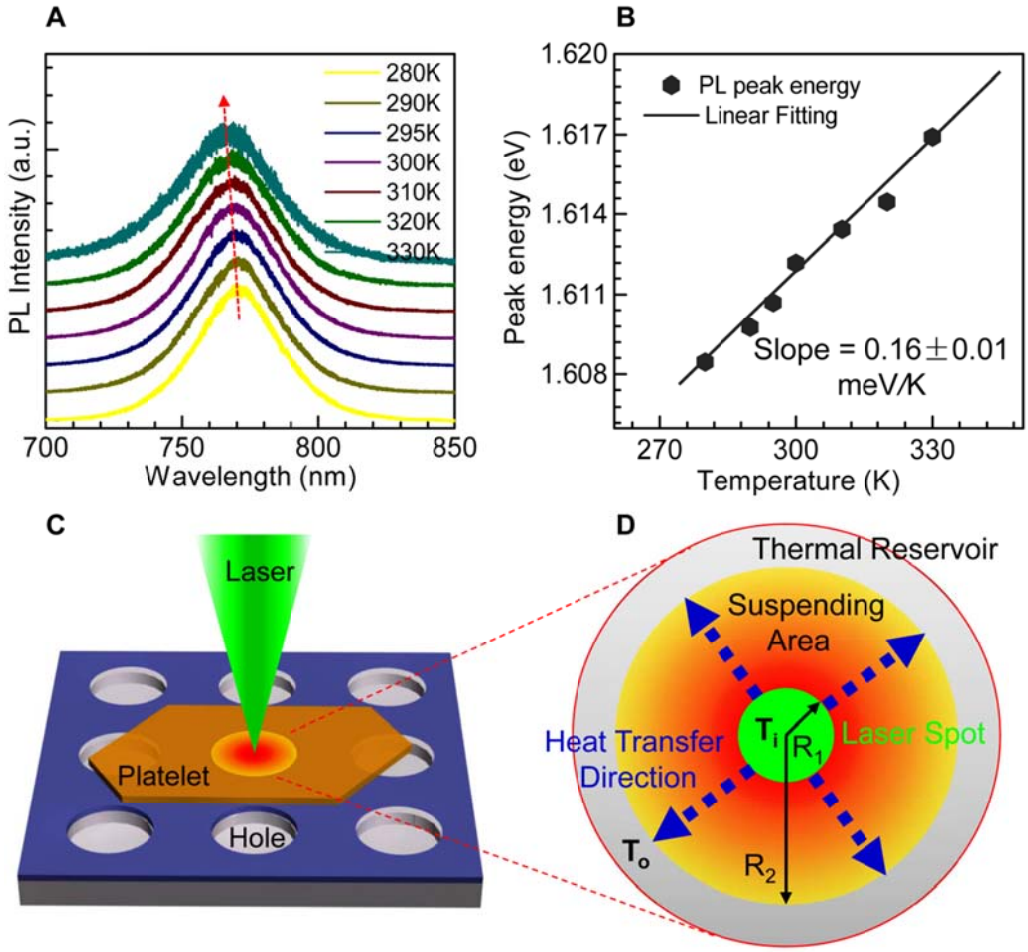

Figure 3 (A) Normalized PL spectra of single $CH_3NH_3PbI_3$ platelets in the temperature range from 280 to 330 K, excited by 532 nm laser at 5 μW. **(B)** The relation between PL emission peaks and the temperature, the peak shift temperature coefficient was obtained through the linear fitting slope. **(C)** Schematic experiment setup for the non-contact thermal conductivity measurement, it shows the excitation laser light focused on a platelet, which is suspended onto holes array on silicon substrate. **(D)** Zoom-in area for deducing the expression suitable for the thermal conductivity extraction for micro sized perovskite. Green spot represents the focused laser. Red area is the suspended area. Gray color area is the heat sink reservoir.

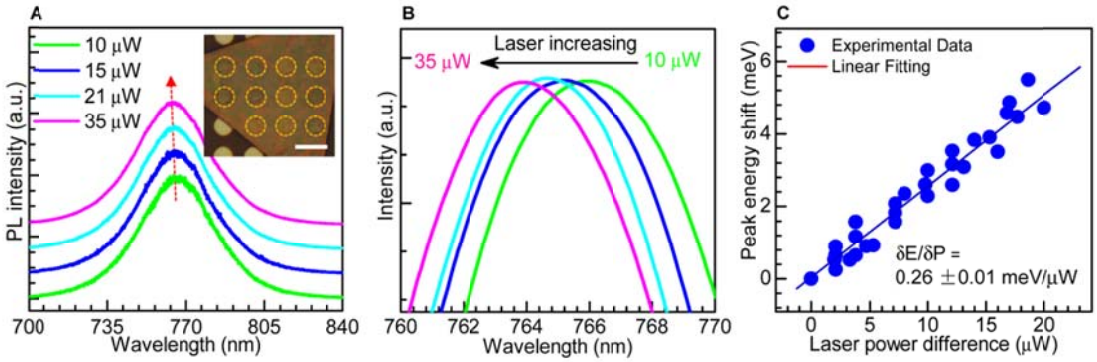

Figure 4 (A) Normalized PL spectra of one typical suspended platelet at different laser power; the laser wavelength is 532 nm. All the spectra except the bottom one are offset vertically for clarity. **(B)** Zoomed PL data of the suspended platelet under different laser powers to show the shift clearly. **(C)** The experimental data and fitting of band edge PL peak energy shift with laser power difference. The spectra were collected from different samples under the laser excitation of 532 nm by using the confocal system. The measurement environment was kept at room temperature.

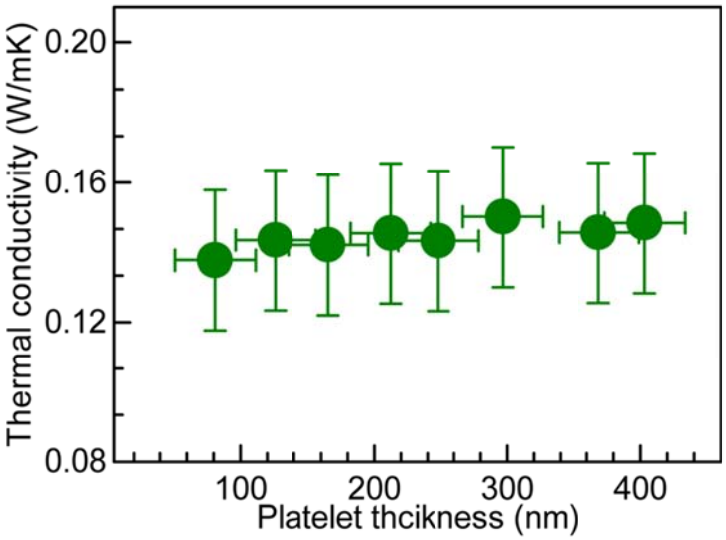

Figure 5 Thickness dependent thermal conductivity values for $CH_3NH_3PbI_3$ platelets. In the range of 80 to 400 nm, the values of thermal conductivity keep almost constant.